PAPER

Check for updates

Green one-pot synthesis of quinoxaline derivatives using sulfo-anthranilic acid functionalized alginate-MCFe$_2$O$_4$ nanostructures: a novel superparamagnetic catalyst with antiproliferative potential†

Ying Lai [iD] * and Ruoyu Zhang*

This study reports a green, multi-component synthesis of 2-aminoimidazole–linked quinoxaline Schiff bases using a novel superparamagnetic acid catalyst. The catalyst consists of sulfo-anthranilic acid (SAA) immobilized on MnCoFe$_2$O$_4$@alginate magnetic nanorods (MNRs), achieving high SAA loading (1.8 mmol g^{-1}) and product yields (91–97%). Characterization of the MCFe$_2$O$_4$@Alginate@SAA MNR catalyst revealed an inverse spinel structure (XRD), a saturation magnetization of 31 emu g^{-1} (VSM), 17.5% organic content (TGA), and a rod-like morphology with diameters of 30–60 nm and lengths of 150–250 nm (SEM). Elemental composition confirmed by EDX analysis indicated successful SAA immobilization and high catalyst purity. The synthesized quinoxaline derivatives were evaluated for antiproliferative activity against SKOV3 and HCT-116 cancer cell lines using the MTT assay. Several compounds, notably **4a**, **4s**, **4t**, **4w**, and **4x**, exhibited potent activity, inhibiting HCT-116 proliferation by >50% at 50 μg mL^{-1}. Compound **4a** demonstrated the most significant inhibition, with 82.3% against SKOV3 cells after 48 h and 69.0% against HCT-116 cells after 24 h, both at 50 μg mL^{-1}. These results suggest the potential of 2-aminoimidazole–linked quinoxaline Schiff bases, particularly **4a**, as promising multi-target chemotherapy agents.

1 Introduction

Cancer is a grave ailment that presently affects people of all ages and has contributed to the escalation of mortality rates worldwide.[1,2] Despite the vast array of anti-cancer medications available, the creation of novel chemotherapeutic agents has persistently posed a remarkable challenge due to their non-selectivity and the propensity of cancerous cells to develop resistance towards existing anti-cancer compounds. Consequently, there is an incessant need to explore better alternatives to cope with these impending challenges.[3] Our research is actively searching for chemical substances that could be developed into novel antitumor agents.[1] Among the compounds of particular interest are imidazole and quinoxaline derivatives.[4–7] These derivatives have recently emerged as a new class of cancer chemotherapeutic agents, demonstrating remarkable efficacy in treating solid tumors.[7,8] It is well-known that imidazole derivatives are potent inhibitors of the epidermal growth factor receptor (EGFR).[9,10] The EGFR is a cellular

transmembrane tyrosine kinase overexpressed in many human tumors, such as breast, ovarian, colon, and prostate.[11–13] The expression levels of EGFR often correlate with vascularity and are associated with poor prognosis in patients.[12] Therefore, inhibitors of EGFR PTK are expected to have tremendous therapeutic potential in treating both malignant and non-malignant epithelial diseases.[14] Several different structural classes of tyrosine kinase inhibitors have been reported and reviewed.[15] Among them, the most promising small-molecule selective EGFR-TK inhibitors include imidazole and quinoxaline.[16,17]

One such example is dacarbazine, an antineoplastic drug containing a 2-aminoimidazole nucleus, which has been utilized for treating cancers such as malignant melanoma, Hodgkin lymphoma, sarcoma, and carcinoma of the pancreas.[17,18] Marine sources have also yielded several 2-aminoimidazole alkaloids, including Namine A, Naamine G, Girolline, and Preclathridine A, that exhibit exceptional anticancer properties (Fig. 1).[19,20] Extensive exploration in the field of tyrosine kinase inhibitors has resulted in the discovery of a plethora of active compounds. In addition to aminoimidazole, quinoxaline have shown effectiveness as selective ATP competitive inhibitors.[17,21] Specifically, AG 1295 and AG 1385 (Fig. 1) are quinoxaline derivatives that block EGFR kinase activity selectively.[22,23] This particular molecule has effectively reversed the

Department of Life Science and Agriculture, Zhoukou Normal University, Zhoukou, Henan 466001, China. E-mail: 20041026@zknu.edu.cn; ruoyzh@163.com

transformed characteristics of sis-transformed NIH 3T3 cells and has demonstrated the ability to slow the growth of C6 glioma-induced tumors in nude mice.[24]

In recent years, there has been an intensified focus on green and sustainable chemistry in the development of novel therapeutic agents. The principles of green chemistry emphasize minimizing hazardous substances and reducing environmental impact during the synthesis of bioactive compounds. Recent studies have highlighted the importance of designing environmentally friendly synthetic routes for producing biologically active molecules, including imidazole and quinoxaline derivatives, which exhibit significant anticancer potential.[25,26] For example, the use of efficient and sustainable catalytic systems for synthesizing quinoxaline derivatives has been reported to yield compounds with enhanced biological activities.[27] Similarly, the integration of green chemistry approaches, such as solvent-free reactions and the utilization of recyclable catalysts, has been demonstrated to improve the overall efficiency and sustainability of the synthesis process.[28,29] These advancements underscore the potential of green synthetic methodologies in addressing the challenges associated with traditional drug development.

A promising strategy for effectively combating cancer, alongside the clinical approach of developing poly-chemotherapy, involves synthesizing hybrid molecules with multiple functional components targeting various biological aspects.[30] In our recent research, we have introduced a novel environmentally friendly synthesis technique and conducted a thorough biological assessment of hybrid molecules consisting of diverse imidazole-based Schiff bases combined with a quinoxaline core.[31] These molecules have significant potential as anti-cancer agents.[10,12]

To evaluate the biological activity of these compounds, we selected two cancer cell lines, HCT-116 and SKOV3, as *in vitro* models. The HCT-116 cell line, derived from human colorectal carcinoma, is widely used in cancer research due to its well-characterized genetic profile, including mutations in key oncogenes such as p53 and K-ras. These genetic alterations make HCT-116 an ideal model for studying the molecular mechanisms of colorectal cancer and assessing the efficacy of anticancer agents.[32] Colorectal cancer is one of the most common and deadly cancers worldwide, further emphasizing the importance of this model in drug discovery studies.
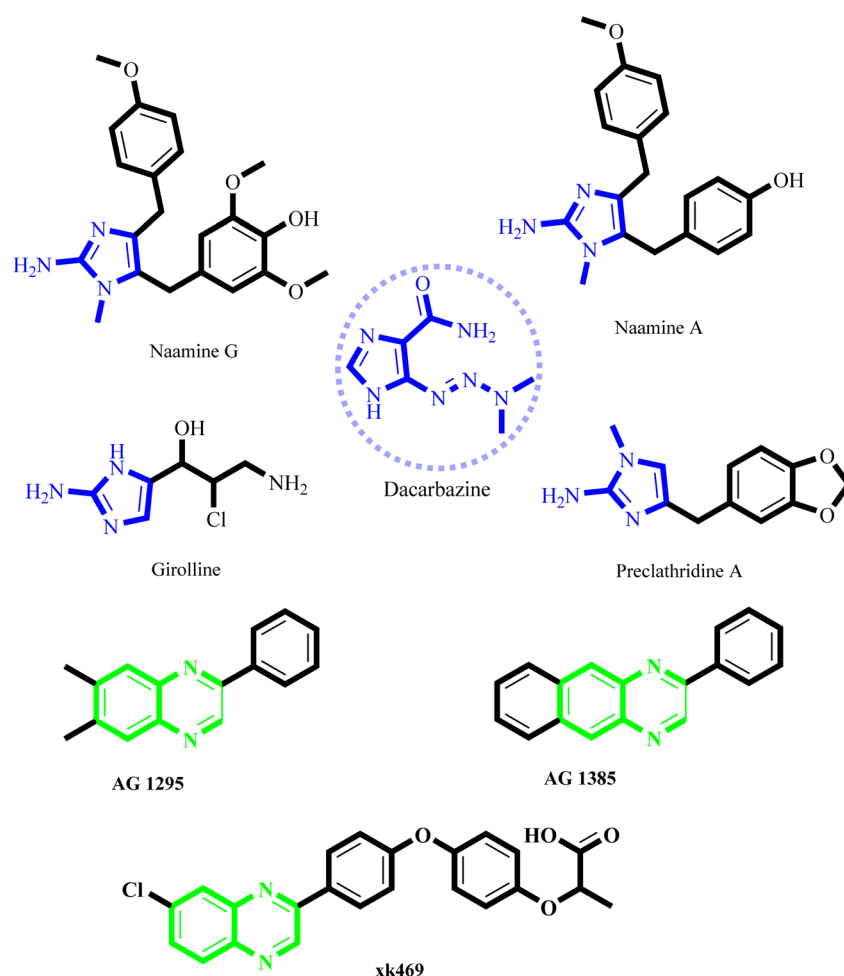

Fig. 1 Some naturally occurring 2-aminoimidazoles and quinoxalines with anti-proliferative activity.

Similarly, the SKOV3 cell line, derived from human ovarian carcinoma, is a well-established model for ovarian cancer research. This cell line is particularly valuable due to its aggressive phenotype, resistance to platinum-based chemotherapy, and ability to mimic the advanced stages of ovarian cancer.[33] Ovarian cancer remains a significant clinical challenge due to its poor prognosis and high mortality rates, making SKOV3 an essential model for evaluating the therapeutic potential of novel compounds. To ensure the selectivity and safety of the synthesized compounds, the HFF (Human Foreskin Fibroblast) cell line was employed as a model for normal, non-cancerous cells. This cell line provides a reliable control for comparing the cytotoxic effects of the compounds on cancerous *versus* healthy cells, thereby enabling the identification of compounds with selective anticancer activity.

What adds to the importance of our research is describing a green synthesis route for producing a highly efficient and leak-free multifunctional heterogeneous magnetic nanocatalyst *via* grafting sulfonic groups onto the surface of $MCFe_2O_4$ MNPs coated with biopolymer layer (alginate) as an efficacious

bridge.[34–37] The alginate layer possesses two functional heads: an OH moiety that strongly binds to the $MCFe_2O_4$ surface hydroxyl groups and COOH groups that bind to the NH group of Sulpho Anthranilic Acid (Scheme 1). Subsequently, we investigated the effectiveness of the newly synthesized organic–inorganic hybrid ($MCFe_2O_4$@Alginate@SAA) as a nanocatalyst with a core–shell structure for synthesizing innovative compounds containing quinoxaline *via* a one-pot cascade reaction. Based on the structural design of these hybrid ligands, significant antiproliferative activities were observed against tumor cell lines derived from human ovaries and colon. The integration of green chemistry principles in this research highlights the potential of sustainable synthetic methodologies in the development of novel anticancer agents.[38–40]

In the current investigation, through the implementation of green synthesis, the substitution pattern was chosen for the disubstituted quinoxaline pharmacophore to create distinct electronic environments that could influence the lipophilicity of the target molecules and, ultimately, their activity. The main aim of generating these hybrids is to strive for the production of
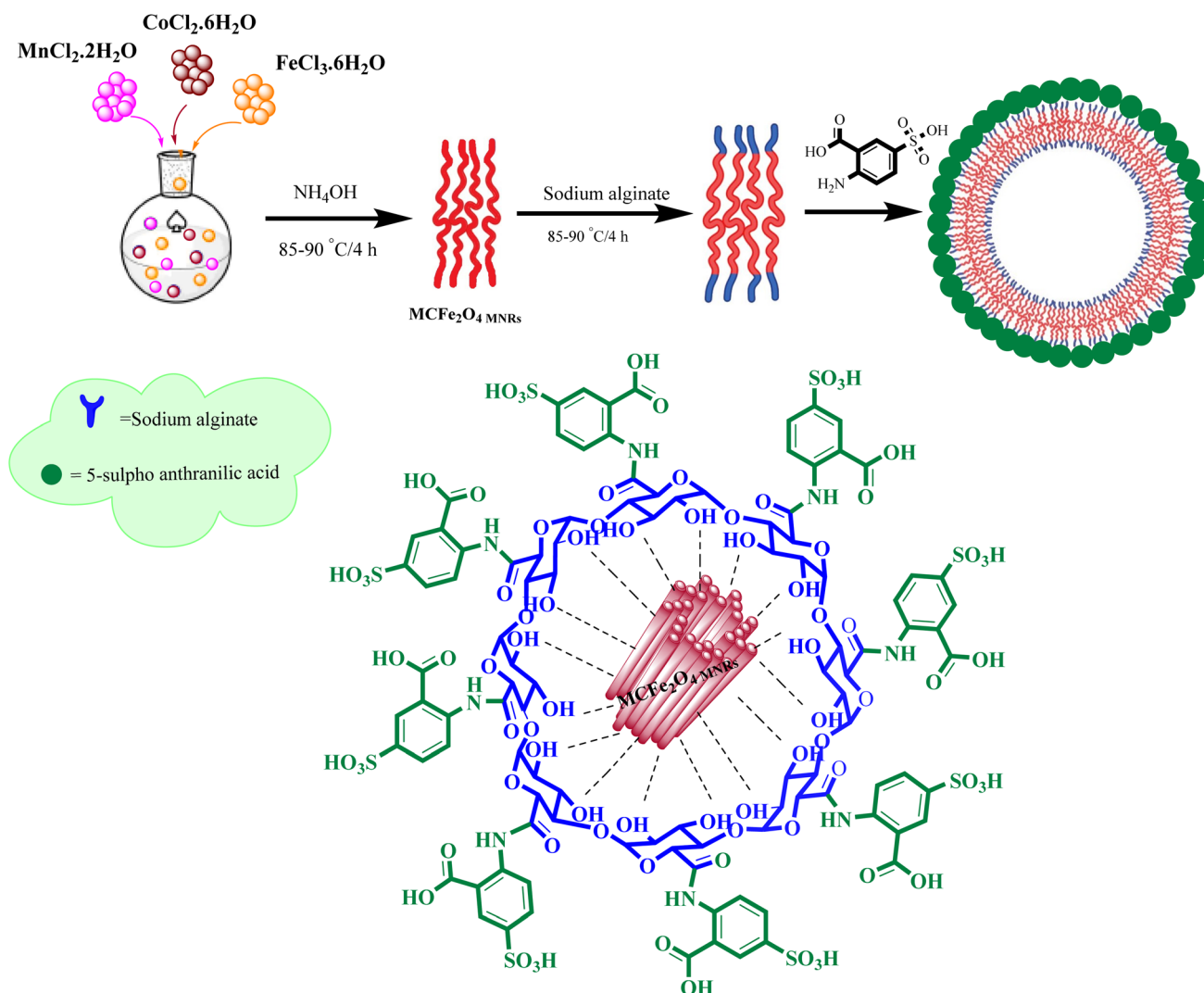
Scheme 1 Synthesis of MCFe₂O₄@Alginate@SAA.

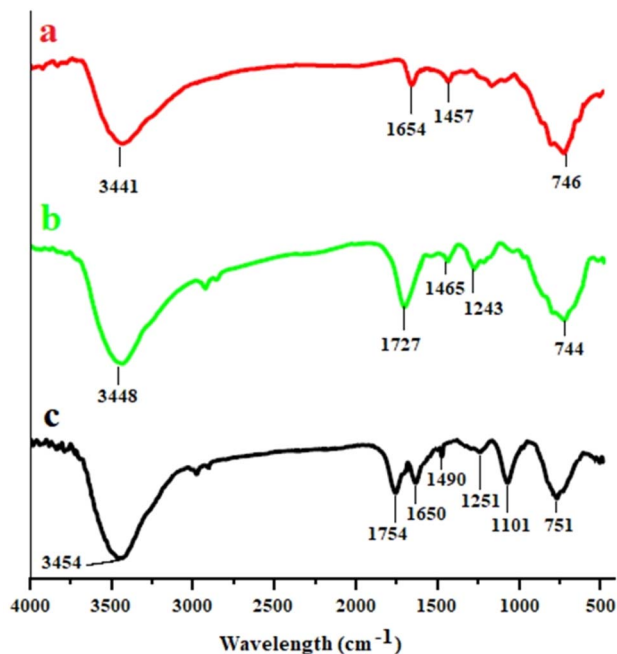Fig. 2 FT-IR spectra: (a) MCFe$_2$O$_4$, (b) MCFe$_2$O$_4$@Alginate and (c) MCFe$_2$O$_4$@Alginate@SAA, and XRD spectra of MCFe$_2$O$_4$ and MCFe$_2$O$_4$@Alginate@SAA.

an efficient antitumor agent with amplified activity and selectivity, specifically towards cancerous cells.

2 Experimental section

2.1 Chemistry

2.1.1 Nanocatalyst preparation. The Mn$_{0.7}$Co$_{0.3}$Fe$_2$O$_4$ MNPs were synthesized using the precipitation method with

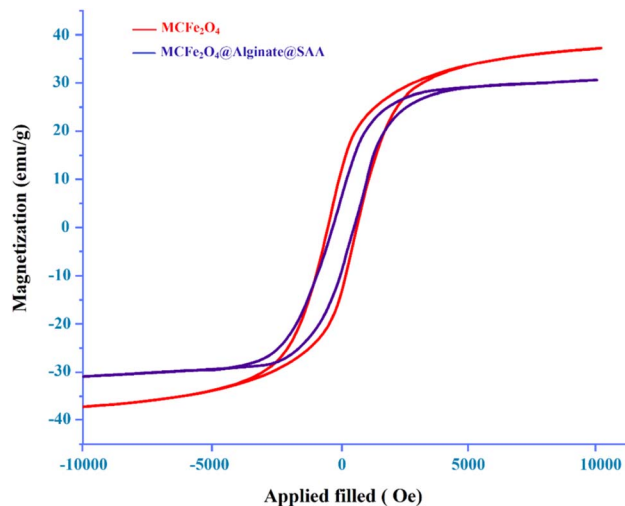Fig. 4 VSM diagrams of MCFe$_2$O$_4$ and MCFe$_2$O$_4$@Alginate@SAA.

FeCl$_3$·6H$_2$O (0.541 g, 2 mmol), MnCl$_2$·2H$_2$O (0.113 g, 0.7 mmol), and CoCl$_2$·6H$_2$O (0.071 g, 0.3 mmol) as starting materials under alkaline and thermal conditions. The three components were dissolved in 100 mL of deionized water while stirring and under N$_2$ atmosphere. NH$_4$OH was slowly added with continuous stirring to result in a brown suspension with a pH of 10–11. The suspension was refluxed for approximately 4 hours, and the resulting brown MCFe$_2$O$_4$ MNPs were magnetically separated, washed with deionized water to remove chloride ions, and dried under vacuum at 70–75 °C for 8 hours. In the next step, the surface of the MC Fe$_2$O$_4$ MNPs was modified with sodium alginate. Firstly, 0.3 g of sodium alginate was dispersed in 50 mL of deionized water through sonication to obtain a homogeneous solution. Next, 1 g of MC Fe$_2$O$_4$ MNPs was dispersed in 50 mL deionized water, and 10 g of the alginate

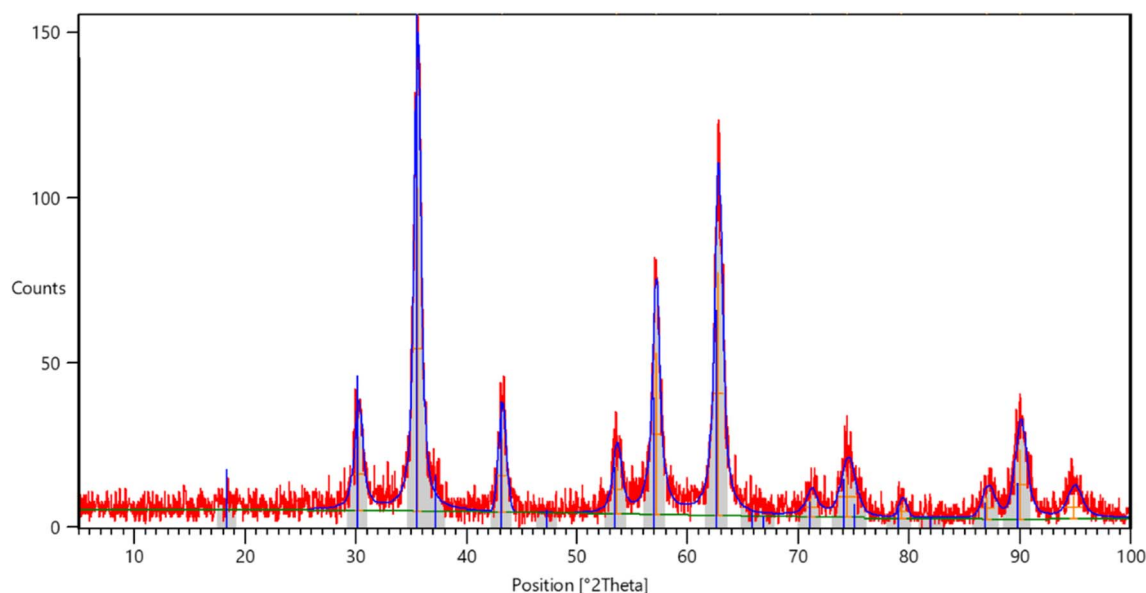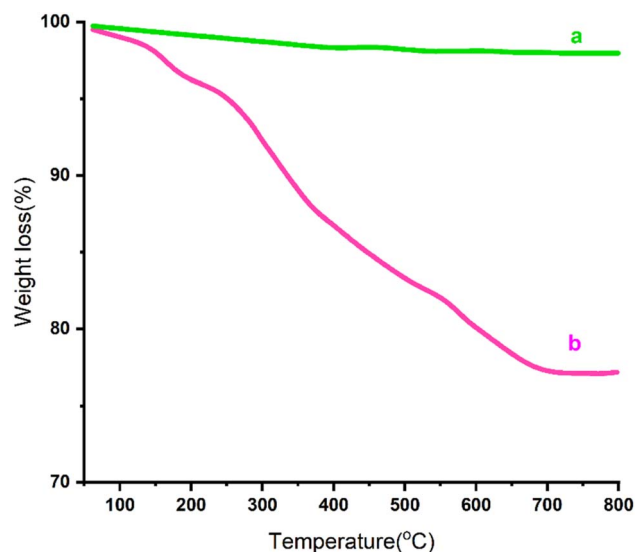Fig. 3 XRD spectra of MCFe$_2$O$_4$@Alginate@SAA.

Fig. 5 TGA spectra of (a) MCFe$_2$O$_4$ and (b) MCFe$_2$O$_4$@Alginate@SAA.

the mixture (monitored by TLC). The resulting reaction mixture was cooled to room temperature, and the crude product was collected by filtration, recrystallized from hot ethanol, and dried at 60 °C under vacuum for 2 h.

2.2 MTT assay

We investigated the potential anti-proliferative effects of 2-aminoimidazole derivatives (compounds **4a–x**) on two human cancer cell lines: HCT-116 (colon cancer) and SK-OV-3 (ovarian cancer). The evaluation was performed using an *in vitro* MTT assay to assess cell viability after treatment with the synthesized compounds. HCT-116 and SK-OV-3 cells were cultured in Dulbecco's Modified Eagle Medium (DMEM) supplemented with 10% fetal bovine serum (FBS) and penicillin–streptomycin (100 U per mL penicillin, 100 μg per mL streptomycin). Cells were maintained at 37 °C in a humidified atmosphere containing 5% CO$_2$. Once the cells reached approximately 70–80% confluence, they were washed with phosphate-buffered saline (PBS, pH 7.4) to remove residual media and detached using 0.25% trypsin–EDTA solution by incubating for 2–5 minutes until cells detached. The trypsinization process was halted by adding complete DMEM, and the cell suspension was centrifuged at 1000 rpm for 5 minutes. The supernatant was discarded, and the cell pellet was resuspended in fresh complete medium. Cell density was determined using a hemocytometer to ensure accurate seeding.

Cells were seeded into 96-well plates at a density of 1×10^4 cells per well in 100 μL of complete DMEM and incubated overnight (approximately 18–24 hours) to allow for cell attachment and recovery. After incubation, the medium was carefully aspirated, and cells were gently washed with PBS to remove any residual FBS. The medium was then replaced with 100 μL of serum-free DMEM to minimize the effects of FBS on drug activity. The 2-aminoimidazole derivatives (compounds **4a–x**) were dissolved in dimethyl sulfoxide (DMSO) to prepare stock solutions. These stock solutions were serially diluted with serum-free DMEM to achieve final concentrations of 5, 10, 50, 100, and 200 μg mL^{-1}. The final concentration of DMSO in any well did not exceed 0.1% (v/v) to avoid solvent-induced cytotoxicity. Imatinib was used as a positive control at equivalent concentrations, and cells treated with 0.1% DMSO in serum-free DMEM served as a negative control. Each concentration

homogeneous solution was gradually added to the MC Fe$_2$O$_4$ suspension. The mixture content was refluxed at 85–90 °C for 12 hours. The alginate-coated MC Fe$_2$O$_4$MNPs were separated using magnetic decantation, washed with water to remove excess unreacted alginate, and dried under vacuum at 60 °C for 6 hours. To synthesize Fe$_2$O$_4$@alginate@Sulpho Anthranilic Acid, 1 g of MC Fe$_2$O$_4$@alginate MNPs was sonicated in *n*-hexane (15 mL) for 30 minutes, followed by the addition of 5-sulpho anthranilic acid (0.5 g) to the cooled MC Fe$_2$O$_4$@alginate suspension. The resulting mixture was stirred at 25 °C for 6 hours. The precipitates were collected using an external magnet, washed three times with ethanol and diethyl ether, and dried under vacuum at 40 °C for 12 hours (Scheme 1).

2.1.2 General procedure for synthesis of new 2-aminoimidazole–quinoxaline derivative (4a–x). In a round-bottomed flask, a mixture of quinoxaline-2-carbaldehyde derivatives (1 mmol), aminoguanidine bicarbonate (1 mmol), α-bromoketones derivative (1 mmol) and 2 mL H$_2$O were heated and stirred at 70 °C in the presence of MCFe$_2$O$_4$@Alginate@SAA (0.03 g) for the times reported in Table 2. Upon the reaction was finished, an external magnet was used to easily separate the catalyst from
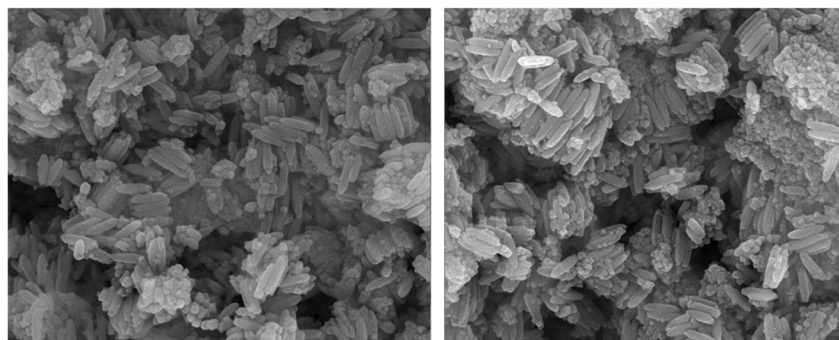

Fig. 6 SEM image of MCFe$_2$O$_4$@Alginate@ SAA.

of the derivatives was tested in triplicate to ensure statistical reliability. Cells were treated with the compounds for 48 hours at 37 °C in a humidified atmosphere containing 5% CO_2.

Following the treatment period, cell viability was assessed using the MTT assay. A fresh MTT solution was prepared at a concentration of 5 mg mL^{-1} in PBS and sterilized by filtration through a 0.22 μm filter to remove any insoluble particles. Twenty microliters of the MTT solution were added to each well, resulting in a final MTT concentration of 0.5 mg mL^{-1}. The plates were incubated for an additional 4 hours at 37 °C in

the dark to allow viable cells to reduce MTT to insoluble purple formazan crystals. After incubation, the supernatant was carefully aspirated without disturbing the formazan crystals. To solubilize the formed crystals, 150 μL of DMSO was added to each well. The plates were gently shaken on an orbital shaker for 10 minutes to ensure complete dissolution of the formazan crystals. The absorbance of each well was then measured at 570 nm using an ELISA plate reader, with a reference wavelength of 630 nm to correct for any background absorbance.
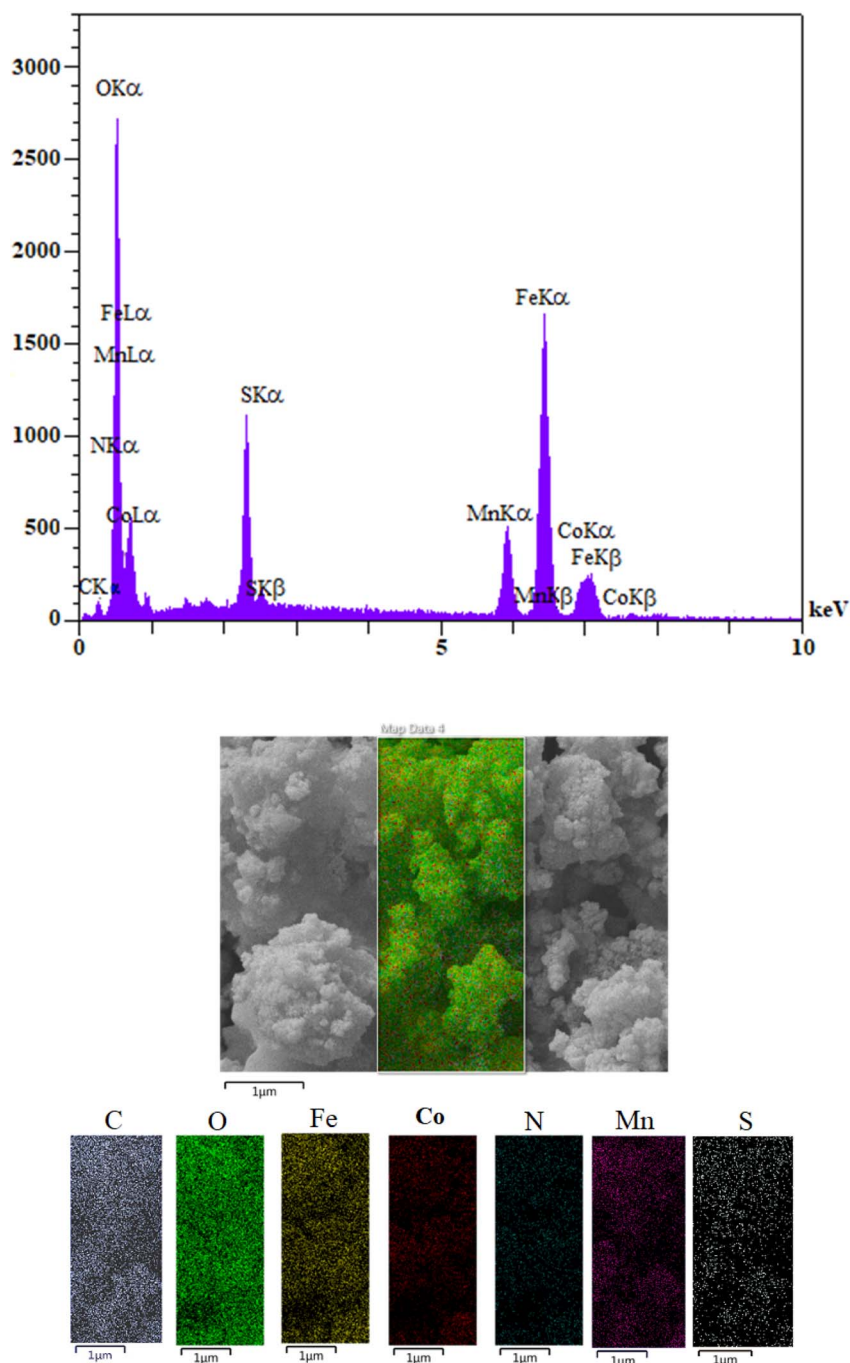

Fig. 7 EDAX spectra of MCFe$_2$O$_4$@Alginate@SAA and the corresponding EDX elemental mapping pattern of the MCFe$_2$O$_4$@Alginate@SAA MNRs.

To evaluate the cytotoxic effects of the compounds on normal cells, human foreskin fibroblast (HFF) cells were cultured and treated under identical conditions as described above for the cancer cell lines. This allowed for a comparative analysis of the selectivity of the compounds towards cancer cells over normal cells. Cell viability was calculated as a percentage of the control using the formula:

$$\text{cell viability (\%)} = (\text{absorbance of treated cells}/\text{absorbance of control cells}) \times 100.$$

Dose–response curves were generated using GraphPad Prism software, and the half-maximal inhibitory concentration (IC_{50}) was determined by nonlinear regression analysis using a sigmoidal dose–response (variable slope) model. All experiments were performed in triplicate, and data were presented as mean ± standard deviation (SD).[41,42]

3 Results and discussion

3.1 Characterization of $MCFe_2O_4$@Alginate@SAA catalyst

The structure of the magnetic ferrite nanocatalyst was characterized using various techniques such as Fourier transform infrared (FT-IR) spectroscopy, X-ray diffraction (XRD), scanning electron microscopy (SEM), transmission electron microscopy (TEM), vibrating sample magnetometry (VSM), energy-dispersive X-ray spectroscopy (EDS) and thermogravimetric analysis (TGA).

The FT-IR spectrum of $MCFe_2O_4$ confirms the formation of $MCFe_2O_4$ nanoparticles, with absorption bands at 3441 cm^{-1} and 746 cm^{-1} corresponding to O–H and metal–oxygen stretching vibrations, respectively. When $MCFe_2O_4$ is decorated with alginate, new peaks appear at 3448 cm^{-1} and 1727 cm^{-1} regions, attributed to the stretching vibrations of O–H and C=O, respectively. Further, the FT-IR spectrum of $MCFe_2O_4$@-Alginate@SAA shows peaks at 1754 cm^{-1} and 1650 cm^{-1}, indicating stretching vibrations of C=O, while a band at 1101 cm^{-1} suggests the presence of S=O. These observations provide evidence of the complexation between the carboxylate moiety of alginate and the NH_2 functional group on the structure of sulfur anthranilic acid (Fig. 2). The X-ray powder diffraction pattern was used to analyze the crystalline structure of the MC Fe_2O_4 and $MCFe_2O_4$@Alginate@SAA MNRs. The diffraction peaks in the XRD spectra confirmed the presence of inverse spinel structures in the nanoparticles. $MCFe_2O_4$ and $MCFe_2O_4$@Alginate@SAA showed characteristic peaks at specific positions, suggesting a robust crystalline spinel ferrite core structure (Fig. 3).

Magnetic properties of $MCFe_2O_4$ and $MCFe_2O_4$ decorated with alginate and SAA were studied using a vibration sample magnetometer (VSM) at room temperature (Fig. 4). Based on the magnetization curve, the saturation magnetization quantity of the $MCFe_2O_4$ MNRs and $MCFe_2O_4$@Alginate@SAA catalyst were measured at approximately 38 emu g^{-1} and 31 emu g^{-1}, respectively. Notably, a decrease in saturation magnetization of $MCFe_2O_4$@Alginate@SAA catalyst is related to the organic compounds (alginate and sulpho anthranilic acid) on the surface of $MCFe_2O_4$ MNRs.

Thermal gravimetric analysis (TGA) was used to investigate the stability and content of coated organic groups on the surface of $MCFe_2O_4$@Alginate@SAA MNRs. The TGA curve showed two weight changes for the nanoparticles. The initial weight loss up to 200 °C was attributed to removing adsorbed solvents and water. The second weight loss at 200–700 °C was due to eliminating grafted organic groups (alginate and sulpho anthranilic acid) from the surface of $MCFe_2O_4$ MNRs. From the TGA curve, it was determined that the amount of organic moiety on the $MCFe_2O_4$@Alginate@SAA MNRs was about 17.5%. Based on this, it was calculated that a high quantity of Alginate@SAA (1.8 mmol g^{-1}) was loaded onto the surface of the $MCFe_2O_4$ magnetic nanoparticles (Fig. 5).

Scanning electron microscopy was applied to evaluate the surface morphology and size of the $MCFe_2O_4$-decorated alginate-functionalized Sulpho Anthranilic Acid ferrite nanoparticles (Fig. 6). As can be seen from SEM images, the morphology of the nanoparticles is rod-like, with a diameter of approximately 30–60 nm and a length of 150–250 nm. It can be concluded that $MCFe_2O_4$@Alginate@SAA is nanorods.

The EDX analysis of the $MCFe_2O_4$@Alginate@SAA magnetic nanocomposite confirmed the presence of Fe, Mn, Co, O, C, N, and S signals and indicates that the $MCFe_2O_4$ structure has
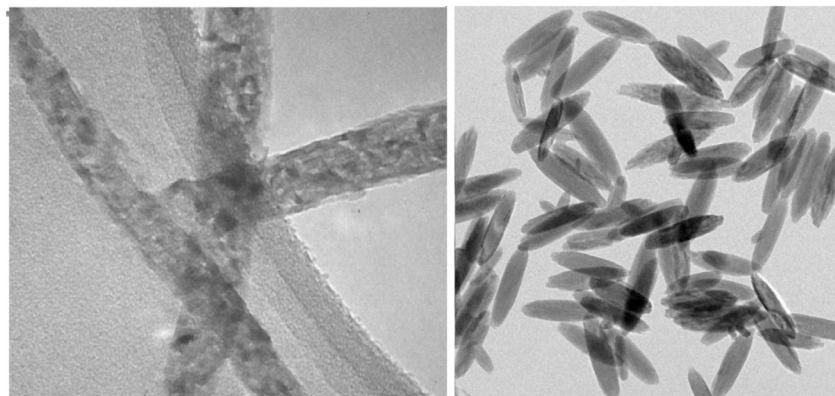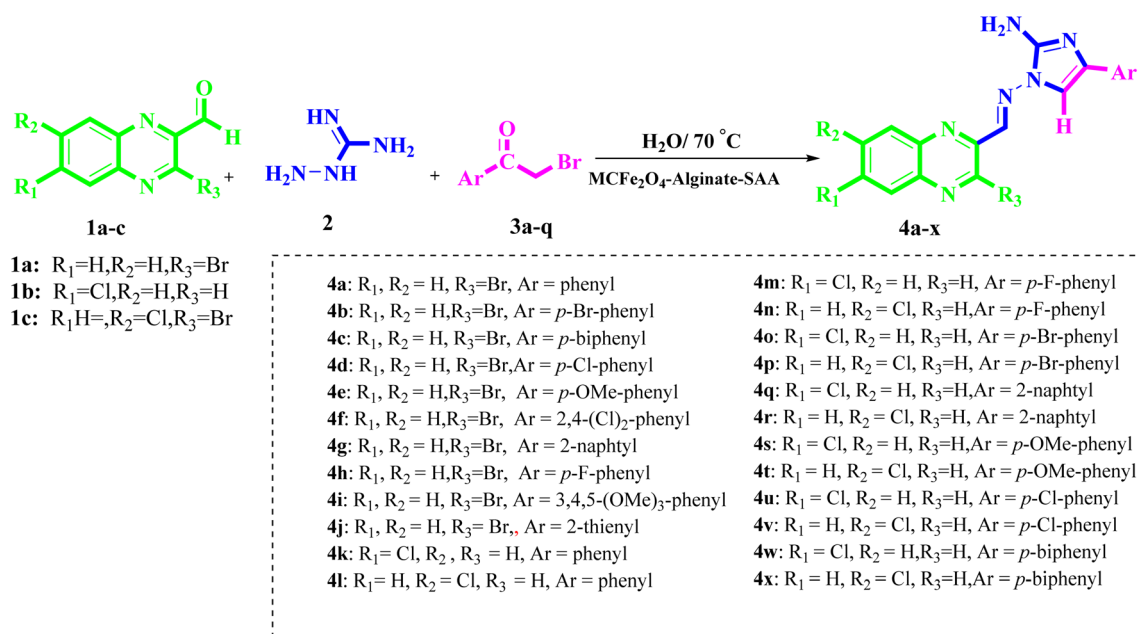

Fig. 8   TEM image of $MCFe_2O_4$@Alginate@SAA.

been successfully decorated with alginate and sulpho anthranilic acid groups. Also, the EDX elemental mapping analysis conforms to the attendance of Mn, Co, S, N, C, O, and Fe in MCFe$_2$O$_4$@Alginate@SAA MNPs. Also, the absence of other elements indicates that MCFe$_2$O$_4$@Alginate@SAA has a high purity level (Fig. 7).

TEM images of the catalyst show that MCFe$_2$O$_4$@Alginate@SAA composite was synthesized in nanorods with an average diameter of about 25 nm and length range of 100–250 nm. Significantly, the TEM result is smaller than the SEM result (Fig. 8).

After characterization of the MCFe$_2$O$_4$@Alginate@SAA catalyst, we have evaluated the catalytic acting of the MCFe$_2$O$_4$@Alginate@SAA in multicomponent reaction for the preparation of functionalized 2-aminoimidazole–quinoxaline hybrids derivatives (Scheme 2).

To explore the optimal reaction conditions for the synthesis of functionalized 2-aminoimidazole–quinoxaline hybrids derivatives, we carried out the three-component coupling quinoxaline-3-bromo-2-carbaldehyde (1 mmol), aminoguanidine bicarbonate (1 mmol), bromo acetophenone (1 mmol) and catalyst (0.1 g) in attendance of ethanol at reflux condition for a specified time as

1a: R$_1$=H,R$_2$=H,R$_3$=Br
1b: R$_1$=Cl,R$_2$=H,R$_3$=H
1c: R$_1$H=,R$_2$=Cl,R$_3$=Br

4a: R$_1$, R$_2$ = H, R$_3$=Br, Ar = phenyl
4b: R$_1$, R$_2$ = H,R$_3$=Br, Ar = p-Br-phenyl
4c: R$_1$, R$_2$ = H, R$_3$=Br, Ar = p-biphenyl
4d: R$_1$, R$_2$ = H, R$_3$=Br,Ar = p-Cl-phenyl
4e: R$_1$, R$_2$ = H,R$_3$=Br, Ar = p-OMe-phenyl
4f: R$_1$, R$_2$ = H,R$_3$=Br, Ar = 2,4-(Cl)$_2$-phenyl
4g: R$_1$, R$_2$ = H,R$_3$=Br, Ar = 2-naphtyl
4h: R$_1$, R$_2$ = H,R$_3$=Br, Ar = p-F-phenyl
4i: R$_1$, R$_2$ = H, R$_3$=Br, Ar = 3,4,5-(OMe)$_3$-phenyl
4j: R$_1$, R$_2$ = H, R$_3$ = Br,, Ar = 2-thienyl
4k: R$_1$= Cl, R$_2$, R$_3$ = H, Ar = phenyl
4l: R$_1$= H, R$_2$ = Cl, R$_3$ = H, Ar = phenyl

4m: R$_1$ = Cl, R$_2$ = H, R$_3$=H, Ar = p-F-phenyl
4n: R$_1$ = H, R$_2$ = Cl, R$_3$=H,Ar = p-F-phenyl
4o: R$_1$ = Cl, R$_2$ = H, R$_3$=H, Ar = p-Br-phenyl
4p: R$_1$ = H, R$_2$ = Cl, R$_3$=H, Ar = p-Br-phenyl
4q: R$_1$ = Cl, R$_2$ = H, R$_3$=H,Ar = 2-naphtyl
4r: R$_1$ = H, R$_2$ = Cl, R$_3$=H, Ar = 2-naphtyl
4s: R$_1$ = Cl, R$_2$ = H, R$_3$=H,Ar = p-OMe-phenyl
4t: R$_1$ = H, R$_2$ = Cl, R$_3$=H, Ar = p-OMe-phenyl
4u: R$_1$ = Cl, R$_2$ = H, R$_3$=H, Ar = p-Cl-phenyl
4v: R$_1$ = H, R$_2$ = Cl, R$_3$=H, Ar = p-Cl-phenyl
4w: R$_1$ = Cl, R$_2$ = H,R$_3$=H, Ar = p-biphenyl
4x: R$_1$ = H, R$_2$ = Cl, R$_3$=H,Ar = p-biphenyl

Scheme 2   Synthesis of functionalized 2-aminoimidazole–quinoxaline hybrids derivatives (**4a–x**).

Table 1   Optimization of reaction conditions for compound **4a**

Entry	Catalyst (g)	Solvent	Condition	Time (min)	Yield[a] (%)
1	SAA (0.1)	EtOH	Reflux	400	74
2	MCFe$_2$O$_4$ (0.1)	EtOH	Reflux	120	37
3	MCFe$_2$O$_4$-Alginate (0.1)	EtOH	Reflux	120	69
4	MCFe$_2$O$_4$-Alginate-SAA (0.1)	EtOH	Reflux	25	86
5	—	EtOH	Reflux	400	0
6	MCFe$_2$O$_4$-Alginate-SAA (0.1)	CH$_3$CN	Reflux	25	73
7	MCFe$_2$O$_4$-Alginate-SAA (0.1)	MeOH	Reflux	25	84
8	MCFe$_2$O$_4$-Alginate-SAA (0.1)	Water	Reflux	25	92
9	MCFe$_2$O$_4$-Alginate-SAA (0.1)	EtOH–H$_2$O (1 : 1)	Reflux	25	89
10	MCFe$_2$O$_4$-Alginate-SAA (0.075)	Water	Reflux	25	92
11	MCFe$_2$O$_4$-Alginate-SAA (0.05)	Water	Reflux	25	92
12	MCFe$_2$O$_4$-Alginate-SAA (0.03)	Water	Reflux	25	92
13	MCFe$_2$O$_4$-Alginate-SAA (0.02)	Water	Reflux	35	81
14	MCFe$_2$O$_4$-Alginate-SAA (0.125)	Water	Reflux	25	92
15	MCFe$_2$O$_4$-Alginate-SAA (0.03)	Water	120 °C	25	97
16	MCFe$_2$O$_4$-Alginate-SAA (0.03)	Water	70 °C	25	97
17	MCFe$_2$O$_4$-Alginate-SAA (0.03)	Water	60 °C	40	84

[a] Isolated yields.

Table 2 One-pot multi-component domino synthesis of quinoxaline derivatives containing 2-aminoimidazole derivatives using MCFe$_2$O$_4$@-Alginate@SAA (0.03 g) as catalyst in H2O at 70 °C

Entry	R1	R2	R3	Ar	Compound	Time (min)	M.P. (°C)	Yield %
1	H	H	Br	Phenyl	**4a**	25	212–215	97
2	H	H	Br	p-Br-phenyl	**4b**	25	262–267	93
3	H	H	Br	p-biphenyl	**4c**	25	201–203	91
4	H	H	Br	p-Cl-phenyl	**4d**	26	261–263	94
5	H	H	Br	p-OMe-phenyl	**4e**	26	226–227	93
6	H	H	Br	2,4-(Cl)$_2$-phenyl	**4f**	24	283–285	93
7	H	H	Br	2-Naphtyl	**4g**	25	239–241	91
8	H	H	Br	p-F-phenyl	**4h**	24	267–269	93
9	H	H	Br	3,4,5-(OMe)$_3$-phenyl	**4i**	25	253–255	92
10	H	H	Br	2-Thienyl	**4j**	26	240–242	93
11	Cl	H	H	Phenyl	**4k**	25	261–263	91
12	H	Cl	H	Phenyl	**4l**	25	258–260	94
13	Cl	H	H	p-F-phenyl	**4m**	24	265–268	91
14	H	Cl	H	p-F-phenyl	**4n**	24	262–265	93
15	Cl	H	H	p-Br-phenyl	**4o**	25	238–240	91
16	H	Cl	H	p-Br-phenyl	**4p**	27	241–243	92
17	Cl	H	H	2-Naphtyl	**4q**	25	272–275	97
18	H	Cl	H	2-Naphtyl	**4r**	25	276–278	94
19	Cl	H	H	p-OMe-phenyl	**4s**	26	241–243	91
20	H	Cl	H	p-OMe-phenyl	**4t**	27	238–240	94
21	Cl	H	H	p-Cl-phenyl	**4u**	30	216–218	91
22	H	Cl	H	p-Cl-phenyl	**4v**	30	222–224	93
23	Cl	H	H	p-Biphenyl	**4w**	25	199–201	97
24	H	Cl	H	p-Biphenyl	**4x**	25	202–204	94

needed to complete the reaction (25 min). Under the optimized condition, the reaction was accomplished by applying different solvents and catalysts, different amounts of catalysts, and a diverse range of temperatures to produce a satisfactory product yield. In order to study the effect of different catalysts on the reaction, a diverse series of catalysts were applied. As can be seen from the results (Table 1), MCFe$_2$O$_4$-Alginate-SAA showed excellent catalytic activity. Evaluation of the reaction under the kind of solvents indicated that water is the most favored solvent because of its considerable efficiency and environmental compatibility. We also optimized the quantity of the catalyst. In nonattendance of MCFe$_2$O$_4$-Alginate-SAA, no product was detected, and starting materials were retrieved without alteration, but using a heterogeneous solid acid catalyst, the satisfactory yield of the favored product was achieved. According to Table 1 (entry 14), it is noticeable that increasing the quantity of catalyst did not have affirmative efficacy on the product yield. It was found that the 30 mg value of MCFe$_2$O$_4$-Alginate-SAA had the best result in the yield.

Moreover, the effect of diverse temperatures was tested on the improvement of the reaction in evidence of a 30 mg quantity of MCFe$_2$O$_4$-Alginate-SAA and H$_2$O as a solvent (Table 1). The best temperature to progress the reaction was selected to be 70 °C. As a final result from Table 1, the best yield and reaction time were obtained when the reaction was carried out in the presence of 0.03 g of MCFe$_2$O$_4$@Alginate@SAA in H$_2$O at 70 °C (97.0%).

Based on optimized reaction conditions, a variety of substituted quinoxaline-2-carbaldehyde was applied to react with aminoguanidine bicarbonate, and an extensive range of substituted α-bromoketones derivatives in the presence of MCFe$_2$O$_4$-Alginate-SAA as a recoverable nanocatalyst at 70 °C to

the synthesis of 2-aminoimidazole–quinoxaline hybrids derivatives (Table 2). The recoverability and reusability of the catalysts are essential advantages in green chemistry and industrial in large-scale operations and commercial applications. In this regard, we also investigated the recyclability of the MCFe$_2$O$_4$@Alginate@SAA in H$_2$O at 70 °C using a selected model reaction of quinoxaline-3-bromo-2-carbaldehyde, aminoguanidine bicarbonate, bromo acetophenone in the presence of MCFe$_2$O$_4$@Alginate@SAA (Table 2, entry 1). After completion of the reaction, the catalyst was easily separated from the reaction mixture using an external magnetic field, washed with hot ethanol, dried at 50 °C for 1 h, and reused in a subsequent similar reaction. The recovered catalyst was reused for seven consecutive cycles without significant loss in its catalytic activity (Fig. 9).
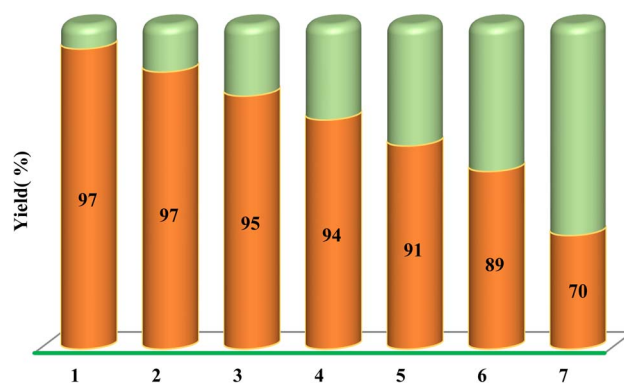

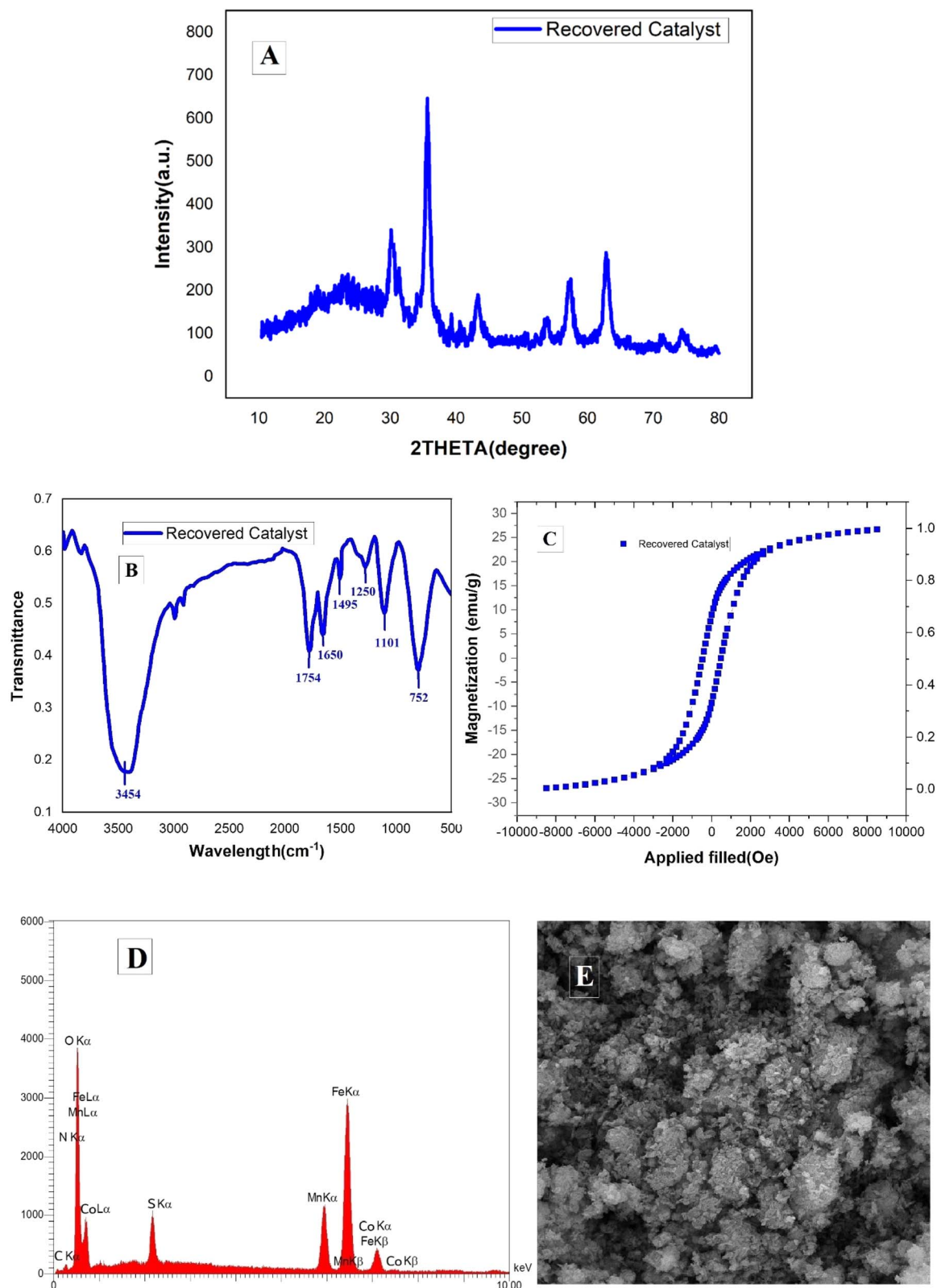**Fig. 9** Reusability of MCFe$_2$O$_4$@Alginate@SAA nanocatalyst.

Fig. 10 (A) XRD, (B) FT-IR, (C) VSM, (D) EDX and, (E) SEM analysis of the recovered $MCFe_2O_4$@Alginate@SAA.

The stability and reusability of the $MCFe_2O_4$@Alginate@SAA magnetic nanocatalyst were extensively evaluated through multiple catalytic cycles for the synthesis of the benzopyrazine–aminoimidazole hybrid compounds. After each catalytic reaction, the nanocatalyst was magnetically separated, washed, and reused in the subsequent cycle. The catalytic activity of the

recovered catalyst remained consistently high even after seven consecutive cycles, demonstrating its excellent stability and recyclability. XRD analysis confirmed that the inverse spinel crystal structure of the $MCFe_2O_4$ nanoparticles was maintained even after the multiple reaction cycles, with no additional peaks observed in the diffraction patterns (Fig. 10A). This suggests the catalyst retained its phase purity and crystallinity.

FT-IR spectroscopy analysis showed no significant changes in the characteristic absorption bands, indicating the preservation of the alginate matrix, metal–oxygen bonds, and immobilized sulfo-anthranilic acid (SAA) moiety (Fig. 10B). VSM studies revealed that the magnetic properties of the nanocatalyst, including the saturation magnetization, remained largely unchanged over the course of the repeated uses. This superparamagnetic behavior enabled the efficient separation and recovery of the catalyst using an external magnetic field (Fig. 10C).

EDX spectroscopy of the recovered catalyst confirmed the presence of all the expected elements, including Mn, Co, Fe, O, C, and S, in comparable ratios to the original catalyst. This observation indicates the stability of the chemical composition of the nanocatalyst after the multiple reaction cycles (Fig. 10D). SEM analyses of the recovered catalyst demonstrated the preservation of the distinctive rod-like morphology of the $MCFe_2O_4$@Alginate@SAA system (Fig. 10E). This observation further substantiates the structural stability of the nanocatalyst under the reaction conditions. The comprehensive characterization of the recovered catalyst confirms the exceptional structural, compositional, and magnetic stability of the $MCFe_2O_4$@Alginate@SAA system, highlighting its potential for efficient and sustainable reuse in multiple catalytic cycles.

The structures of the desired compounds were analyzed through various spectroscopic techniques, including FTIR spectroscopy, ^{1}H NMR, ^{13}C NMR, two-dimensional nuclear magnetic resonance spectroscopy (2D NMR) using heteronuclear single quantum coherence (HSQC), correlation spectroscopy (COSY), heteronuclear multiple bond correlation (HMBC), and rotating-frame Overhauser effect spectroscopy (ROESY) as well as mass spectrometry. The 2D NMR spectra were particularly informative for several synthesized final compounds, namely **4d**, **4m**, and **4n**. In particular, the ROESY spectrum obtained for compound **4d** in 2D NMR explicitly confirmed the final derivatives' E-geometry. More specifically, correlations between the hydrogen on HC=N (imine) with **H-5** imidazole, NH_2, and **H-3′** in the quinoxaline ring were observed in this spectrum, confirming the compound's E-geometry.

Table 3 The inhibitory growth percentages of the compounds **4a**, **4e**, **4j**, **4k**, **4l**, **4m**, **4n**, **4s**, **4s**, **4t**, **4w**, and **4x** were assessed on selected tumor cell lines and a standard cell line at concentrations of 10 and 50 μg mL^{-1} for 24 hours

Compounds	HCT-116[a]		SKOV3		HFF	
	50 μg mL^{-1}	10 μg mL^{-1}	50 μg mL^{-1}	10 μg mL^{-1}	50 μg mL^{-1}	10 μg mL^{-1}
4a	69.0 ± 7.4	45.6 ± 3.4	62.8 ± 4.1	40.3 ± 6.5	34.7 ± 1.6	5.2 ± 2.3
4e	24.0 ± 3.6	8.2 ± 2.0	33.0 ± 3.0	8.2 ± 1.2	7.13 ± 1.5	—
4j	46.8 ± 4.5	32.0 ± 6.1	—	—	nt[b]	nt
4k	30.0 ± 1.2	13.3 ± 1.2	28.1 ± 2.1	7.0 ± 0.2	31.3 ± 3.6	—
4l	31.6 ± 2.8	13.7 ± 1.9	27.2 ± 4.2	8.2 ± 0.8	28.4 ± 7.6	—
4m	29.0 ± 8.2	16.3 ± 5.1	—	—	40.66 ± 11.2	—
4n	30.7 ± 3.0	14.2 ± 9.5	—	—	38.0 ± 5.3	—
4s	70.6 ± 7.5	35.4 ± 6.1	59.0 ± 4.1	20.0 ± 6.7	51.0 ± 14.2	—
4t	69.2 ± 6.0	36.5 ± 2.7	61.3 ± 1.3	21.1 ± 5.2	49.5 ± 6.8	—
4w	32.0 ± 1.8	21.8 ± 5.2	43.3 ± 3.8	7.5 ± 0.9	—	—
4x	31.3 ± 71	21.0 ± 2.3	44.1 ± 6.2	8.1 ± 3.7	—	—
Imatinib	83.0 ± 6.1	50.0 ± 14.1	85.2 ± 7.4	42.5 ± 7.1	87.7 ± 7.4	25.2 ± 0.9

[a] Percent inhibition of cell proliferation at different concentrations. [b] Not tested.

Table 4 The inhibitory growth percentages of the compounds **4a**, **4k**, **4l**, **4s**, **4t**, **4w**, and **4x** for the selected tumor cell lines at 10 and 50 μg mL^{-1} (48 h)

Compounds	HCT-116		SKOV3		HFF	
	50 μg mL^{-1}	10 μg mL^{-1}	50 μg mL^{-1}	10 μg mL^{-1}	50 μg mL^{-1}	10 μg mL^{-1}
4a	64.3 ± 1.3	51.0 ± 3.2	82.3 ± 7.8	47.3 ± 5.4	36.6 ± 6.5	32.5 ± 2.9
4k	34.0 ± 2.1	4.1 ± 0.8	32.3 ± 1.6	—	18.5 ± 7.3	9.2 ± 3.6
4l	35.7 ± 2.8	6.1 ± 4.1	31.5 ± 5.2	—	15.5 ± 5.1	8.5 ± 2.5
4s	77.2 ± 4.2	3.2 ± 5.2	57.3 ± 8.9	16.6 ± 4.8	15.3 ± 4.2	8.0 ± 1.7
4t	76.5 ± 12.4	3.7 ± 1.9	55.6 ± 3.4	17.5 ± 2.5	14.9 ± 1.9	9.1 ± 2.4
4w	51.0 ± 3.5	37.7 ± 8.2	33.3 ± 3.9	16.6 ± 1.5	23.0 ± 3.2	14.0 ± 4.2
4x	52.0 ± 7.2	39.4 ± 1.2	32.1 ± 6.4	18.0 ± 4.8	21.9 ± 1.5	17.1 ± 5.3
Imatinib	96.5 ± 6.2	73.5 ± 9.2	93.5 ± 14.5	66.5 ± 8.2	81.2 ± 9.2	63.4 ± 7.3

Notably, only within the E-geometry of this compound could interpretations be made regarding the correlations between the hydrogen of the imine, imidazole **H-5**, and NH_2—a selective long-range HMBC correlation of compound **4x**.

We successfully employed plate chromatography to obtain high-purity samples of 24 compounds (**4a–x**) and confirmed their geometries using a range of spectroscopic techniques, including ^{1}H-NMR, ^{13}C-NMR, HSQC, COSY, ROESY, and HMBC. The COSY spectra of compounds **4m** and **4n** revealed two signals at δ 7.74 and 8.15 ppm in both cases, indicating the presence of protons 2″ and 6″ at δ 7.74 ppm that correlated with H3″ and H5″ at δ 7.20 ppm for the first signal, and H8′ at 8.15 ppm that correlated with H7′ at 7.95 ppm for the second signal (Fig. 8s†). These findings confirmed the presence of a chlorine atom at the H6′-position in the quinoxaline ring of compound **4m** and at

the H7′-position in compound **4n**. Additionally, we presented selective long-range HMBC correlations for compound **4a** in Fig. S1 and S2.†

3.1.1 Colorimetric MTT cell viability assay: anti-proliferation effects and selective toxicity of the tested 2-aminoimidazole–quinoxaline hybrids *vs.* Imatinib. The anti-proliferative activity of a series of 2-aminoimidazole derivatives (**4a–x**) was assessed against two cancer cell lines, SKOV3 (human ovarian carcinoma) and HCT116 (human colon cancer). To determine the selectivity of their cytotoxic effects on cancer cells compared to normal cells, tests were also conducted on HFF (human foreskin fibroblasts) normal cells. Treatment involved exposing cells to increasing concentrations (5, 10, 50, 100, and 200 μg mL^{-1}) of each compound, while imatinib served as the standard positive control during the
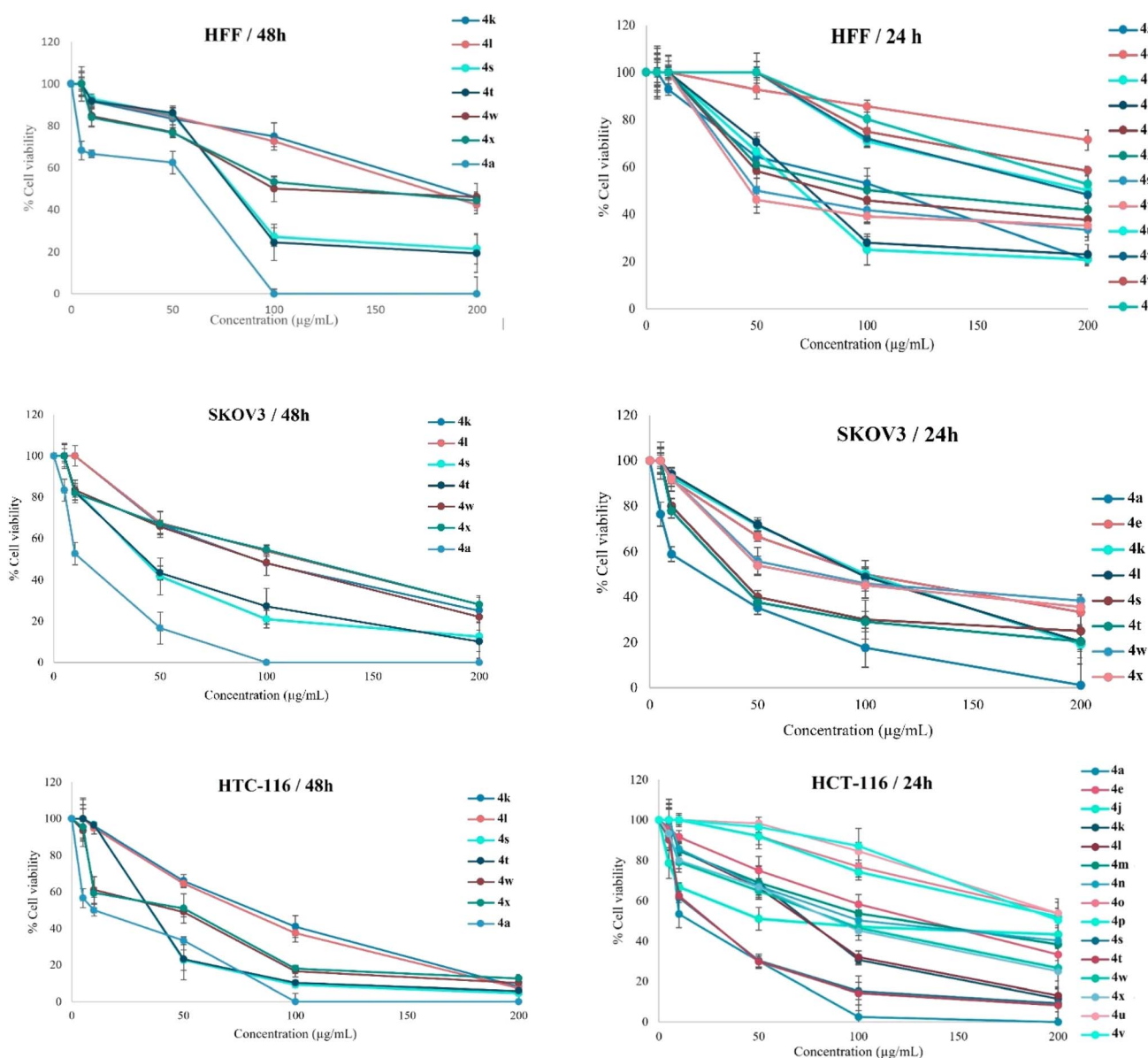

Fig. 11 Anti-proliferative activity of the compounds in SKOV3, HCT-116, and HFF cell lines, at the concentrations of 5, 10, 50, 100, and 200 μg mL^{-1} after 24 h and 48 h.
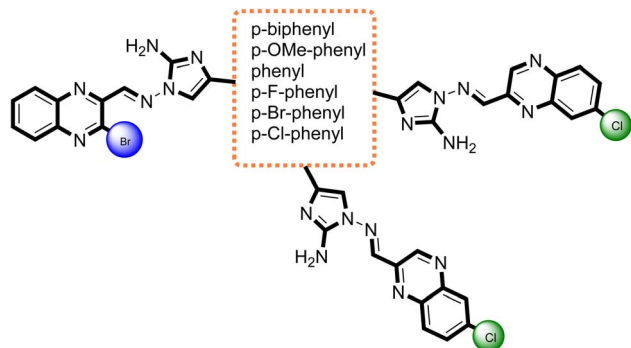
Fig. 12 A visual depiction illustrating the relationship between the chemical structure and biological activity of quinoxaline derivatives.

biological evaluation process. Cell viability was evaluated using the [3-(4,5-dimethylthiazol-2-yl)-2,5-diphenyltetrazolium bromide] (MTT) colorimetric assay after incubation periods of 24 and 48 hours (Tables 3 and 4). IC_{50} values and cell viability for different concentrations (ranging from 5 to 200 μM) of the 2-aminoimidazole derivatives were calculated using a graphical method described in Scheme 2.

The provided data offers valuable insights into the effectiveness and potency of the tested compounds. The values presented represent the mean value plus or minus the standard deviation derived from at least three independent experiments with consistent results. A control group of DMSO ($n = 2 \pm$ SEM) was incorporated for each cell line under examination. Graph-Pad Prism 8 generated a standard graph, plotting the drug concentration on the X-axis and relative cell viability on the Y-axis (Fig. 11). Cell viability (%) was calculated based on the Mean OD/Control OD ratio multiplied by 100%.

3.1.2 Structure–activity relationship. As indicated in (Tables 3 and 4) among compounds (**4a–4j**), **4a** (phenyl), and **4e** (*p*-OMe-phenyl) proved to be active against SKOV3 and HCT-116

cell lines. Generally, adding a Cl atom in derivative (**4k–y**) reduced tumor cell viability. After 24 hours, several compounds **4a**, **4e**, **4j**, **4k**, **4l**, **4m**, **4n**, **4s**, **4t**, **4w**, and **4x**, demonstrated inhibition percentages ranging from 25% to 70% against the proliferation of HCT-116 cells when administered at a concentration of 50 μg mL^{-1}. Additionally, for 24 and 48 hours, compounds **4a**, **4s**, and **4t** inhibited human colon cancer cell proliferation at a concentration of 50 μg mL^{-1} with a percentage of inhibition more significant than 65%. After 48 hours of observation, compound **4a** was found to have the most significant inhibition rate of 82.3% at a concentration of 50 μg mL^{-1} against SKOV3 cells. Compound **4a** exhibited significant growth inhibitory effects against SKOV3 and HCT-116 cells, with inhibition rates exceeding 40% at a concentration of 10 μg mL^{-1}. Compared to imatinib, a standard drug, compound **4a** was less detrimental to the HFF cell line after 24 hours, as indicated in Table 3. In the pursuit of modifying substituents, the phenyl group has been After 48 hours of observation, compound **4a** had the most significant inhibition rate of 82.3% at a concentration of 50 μg mL^{-1} against SKOV3 cells. Compound **4a** exhibited significant growth inhibitory effects against SKOV3 and HCT-116 cells, with inhibition rates exceeding 40% at a concentration of 10 μg mL^{-1}. Compared to imatinib, a standard drug, compound **4a** was less detrimental to the HFF cell line after 24 hours, as indicated in Table 3. It was identified as a preferred substitute for hindering the growth of cell lines, particularly HCT-116 and SKOV3. It has been observed that the anticancer activity against cancer cell lines can be reduced by altering the electronic environment of the phenyl ring by introducing groups that either donate or withdraw electrons (**4a–j**). However, this approach has yielded promising results in maintaining an acceptable safety profile for standard cell lines after 24 hours. On the other hand, the inclusion of a chlorine atom at either the 6- or 7-position and a bromine atom at the 3-position of the quinoxaline ring has been shown to increase the anticancer activity against HCT-116 and SKOV3 cell lines after
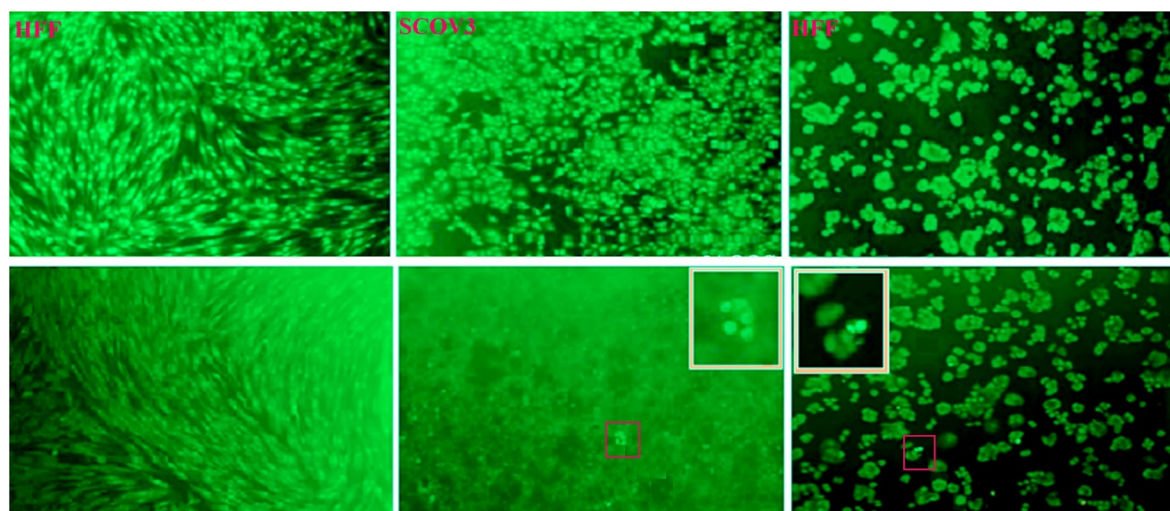

Fig. 13 Compound **4a** was subjected to AO/EB staining under different conditions: DMSO 1% as a negative control, and treatment with 5 μg mL^{-1} after 24 hours.

48 hours. The Cl-quinoxaline series (**4k–x**) has revealed that compounds such as *p*-OMe-phenyl, *p*-biphenyl, and phenyl exhibited superior activity against both HCT-116 and SKOV3 cell lines compared to other compounds (Fig. 12).

3.1.3 AO/EB staining. To differentiate between apoptotic, necrotic, and live cells under a fluorescent microscope, the acridine orange/ethidium bromide (AO/EB) fluorescent staining assay. Acridine orange (AO) can permeate either alive or dead cells, even if they have intact membranes. AO's ability to bind to DNA through intercalation or electrostatic attraction causes the cells to fluoresce green. Conversely, ethidium bromide (EB) has a more limited staining capability, as it can only penetrate cells with compromised membrane integrity. When EB binds to DNA through electrostatic attraction, it produces an orange fluorescence in the nucleus. During this investigation, HCT 116, SKOV3, and HFF cells were subjected to varying concentrations of compound **4a** (100, 50, 25, 5, and 1 µg mL^{-1}) for 24 hours. The results indicate that the cells in the control group maintained their normal morphology and exhibited a green hue (Fig. 13). The administered compound **4a** resulted in alterations in cellular characteristics and pigmentation, along with modifications in their physical constitution, including the formation of membrane blebs, condensation of chromatin, reduction in cell size, and the creation of structures associated with apoptosis (Fig. 13). These observations indicate that compound **8a** led to the demise of HCT-116 and SKOV3 cells. The present study revealed a noteworthy rise in the rate of programmed cell death, also known as apoptosis, in cell lines HCT-116 and SKOV3 upon administration of compound **4a** at a concentration of 5 µg mL^{-1} after 24 hours; this suggests that the treatment brought about a state of induced apoptosis.

4 Conclusions

A novel magnetic core–shell nanorod catalyst, MCFe$_2$O$_4$@-Alginate@SAA, was developed and successfully employed in a green, multi-component synthesis of 2-aminoimidazole–quinoxaline hybrids. This sustainable approach circumvents the limitations of conventional methods, offering a cost-effective, non-toxic, and easily recoverable catalyst with reusable catalytic activity. Evaluation of the synthesized compounds against HCT-116 and SKOV3 cancer cell lines revealed promising antiproliferative activity, particularly for compound **4a**, which induced apoptosis in both cell lines. These findings highlight the potential of these quinoxaline derivatives, especially **4a**, as lead compounds for anticancer drug development.

Data availability

All data generated or analyzed during this study are included in this published article and data will be made available on request.

Authors contribution

Ruoyu Zhang: supervision – Ruoyu Zhang played a pivotal role in overseeing the research project, providing strategic direction, guidance, and insight throughout the course of the study. His contributions included defining the key objectives, designing the study methodology, and maintaining the project timeline. Ying Lai: draft preparation – Ying Lai was instrumental in drafting the manuscript, articulating the findings from the research, and presenting the data in a clear, coherent manner. This role involved extensive literature review, data analysis, and interpretation of the results within the context of the research objectives.

Conflicts of interest

The authors declare that they have no known competing financial interests or personal relationships that could have appeared to influence the work reported in this paper.

References

1 C. Fitzmaurice, C. Allen, R. M. Barber, L. Barregard, Z. A. Bhutta, H. Brenner, D. J. Dicker, O. Chimed-Orchir and R. Dandona, *JAMA Oncol.*, 2017, **3**, 524–548.
2 A. G. Waks and E. P. Winer, *JAMA*, 2019, **321**, 288–300.
3 J. Zugazagoitia, C. Guedes, S. Ponce, I. Ferrer, S. Molina-Pinelo and L. Paz-Ares, *Clin. Ther.*, 2016, **38**, 1551–1566.
4 M. N. Noolvi, H. M. Patel, V. Bhardwaj and A. Chauhan, *Eur. J. Med. Chem.*, 2011, **46**, 2327–2346.
5 M. Iradyan, N. Iradyan, G. Stepanyan, F. Arsenyan and B. Garibdzhanyan, *Pharm. Chem. J.*, 2010, **44**, 175–182.
6 K. Shalini, P. K. Sharma and N. Kumar, *Chem. Sin.*, 2010, **1**, 36–47.
7 S. T. Al-Rashood, I. A. Aboldahab, M. N. Nagi, L. A. Abouzeid, A. A. Abdel-Aziz, S. G. Abdel-Hamide, K. M. Youssef, A. M. Al-Obaid and H. I. El-Subbagh, *Bioorg. Med. Chem.*, 2006, **14**, 8608–8621.
8 F. A. Al-Omary, L. A. Abou-Zeid, M. N. Nagi, E.-S. E. Habib, A.-M. Alaa, A. S. El-Azab, S. G. Abdel-Hamide, M. A. Al-Omar, A. M. Al-Obaid and H. I. El-Subbagh, *Bioorg. Med. Chem.*, 2010, **18**, 2849–2863.
9 S. Kalra, G. Joshi, M. Kumar, S. Arora, H. Kaur, S. Singh, A. Munshi and R. Kumar, *RSC Med. Chem.*, 2020, **11**, 923–939.
10 A. Ayati, S. Moghimi, S. Salarinejad, M. Safavi, B. Pouramiri and A. Foroumadi, *Bioorg. Chem.*, 2020, **99**, 103811.
11 S.-C. Wang and M.-C. Hung, *Clin. Cancer Res.*, 2009, **15**, 6484–6489.
12 E. S. Kim, *J. Natl. Compr. Cancer Network*, 2003, **1**, S87–S95.
13 A. E. Maennling, M. K. Tur, M. Niebert, T. Klockenbring, F. Zeppernick, S. Gattenlöhner, I. Meinhold-Heerlein and A. F. Hussain, *Cancers*, 2019, **11**, 1826.
14 F. Dehnavi, M. Akhavan and A. Bekhradnia, *RSC Adv.*, 2024, **14**, 35400–35423.
15 S. Yadav, D. Sinha, S. K. Singh and V. K. Singh, *Chem. Biol. Drug Des.*, 2012, **80**, 625–630.
16 R. Pal, G. Teli, G. S. P. Matada and P. S. Dhiwar, *J. Mol. Struct.*, 2023, 136021.
17 R. Pal, G. Teli, G. S. P. Matada and P. S. Dhiwar, *ChemistrySelect*, 2023, **8**, e202301200.

18 G. Chawla, O. Gupta and T. Pradhan, *ChemistrySelect*, 2023, **8**, e202301401.

19 P. B. Koswatta and C. J. Lovely, *Nat. Prod. Rep.*, 2011, **28**, 511–528.

20 D. S. Ermolat'ev, J. B. Bariwal, H. P. Steenackers, S. C. De Keersmaecker and E. V. Van der Eycken, *Angew. Chem.*, 2010, **122**, 9655–9658.

21 T. Kaushal, G. Srivastava, A. Sharma and A. S. Negi, *Bioorg. Med. Chem.*, 2019, **27**, 16–35.

22 R. R. E. Eldin, A. A. Al-Karmalawy, M. H. Alotaibi and M. A. Saleh, *New J. Chem.*, 2022, **46**, 9975–9984.

23 F. Ciardiello, *Drugs*, 2000, **60**, 25–32.

24 K. Sugita, K. Koizumi and H. Yoshida, *Cancer Res.*, 1992, **52**, 168–172.

25 A. Das and A. K. Das, *New J. Chem.*, 2023, **47**, 5347–5355.

26 A. K. Das, S. Nandy and S. Bhar, *RSC Adv.*, 2022, **12**, 4605–4614.

27 F. Maryani and A. W. Septama, *Biomater. Adv.*, 2022, **3**, 8267–8275.

28 A. Das, D. Chavda, M. Manna and A. K. Das, *New J. Chem.*, 2024, **48**, 18249–18260.

29 A. K. Das, M. S. Ali, A. Misra, S. Islam, B. Kar, S. Biswas, G. Ghatak, D. Mal, M. Shit and M. Dolai, *Appl. Organomet. Chem.*, 2024, e7796.

30 E. Boggio, C. L. Gigliotti, I. Stoppa, D. Pantham, S. Sacchetti, R. Rolla, M. Grattarola, C. Monge, S. Pizzimenti and U. Dianzani, *Pharmaceutics*, 2023, **15**, 937.

31 M. Akhavan, N. Foroughifar, H. Pasdar and A. Bekhradnia, *J. Mazandaran Univ. Med. Sci.*, 2020, **29**, 82–90.

32 S. Cruz, S. E. Gomes, P. M. Borralho, C. M. Rodrigues, S. P. Gaudêncio and F. Pereira, *Biomolecules*, 2018, **8**, 56.

33 A. Hallas-Potts, J. C. Dawson and C. S. Herrington, *Sci. Rep.*, 2019, **9**, 5515.

34 M. Akhavan and A. Bekhradnia, *RSC Adv.*, 2021, **11**, 14755–14768.

35 M. Akhavan, N. Foroughifar, H. Pasdar and A. Bekhradnia, *Comb. Chem. High Throughput Screening*, 2019, **22**, 716–727.

36 Z. Esam, M. Akhavan, A. Bekhradnia, M. Mohammadi and S. Tourani, *Catal. Lett.*, 2020, **150**, 3112–3131.

37 M. Akhavan, N. Foroughifar, H. Pasdar, A. Khajeh-Amiri and A. Bekhradnia, *Transition Met. Chem.*, 2017, **42**, 543–552.

38 A. Rana, S. Pathak, K. Kumar, A. Kumari, S. Chopra, M. Kumar, D. Kamil, R. Srivastava, S.-K. Kim and R. Verma, *Biomater. Adv.*, 2024, **5**, 2767–2784.

39 A. K. Das, N. Sepay, S. Nandy, A. Ghatak and S. Bhar, *Tetrahedron Lett.*, 2020, **61**, 152231.

40 M. Akhavan, Z. Esam, A. Mirshafa, M. Lotfi, S. Pourmand, F. Ashori, M. Rabani, G. Ekbatani, S. Tourani and R. Beheshti, *RSC Adv.*, 2024, **14**, 22916–22938.

41 D. Gerlier and N. Thomasset, *J. Immunol. Methods*, 1986, **94**, 57–63.

42 P. W. Sylvester, *Drug Design and Discovery: Methods and Protocols*, 2011, pp. 157–168.